Histology-based quantification of boiling histotripsy outcomes via ResNet-18 network: towards mechanical dose metrics

Ekaterina Ponomarchuk [a,*], Gilles Thomas [b], Minho Song [c], Alisa Krokhmal [a], Anastasia Kvashennikova [a], Yak-Nam Wang [b], Vera Khokhlova [a,b], Tatiana Khokhlova [c]

[a] *Physics Faculty, Lomonosov Moscow State University, Moscow, Russian Federation*
[b] *Center for Industrial and Medical Ultrasound, University of Washington, Seattle, United States of America*
[c] *Department of Gastroenterology, University of Washington, Seattle, United States of America*

* Corresponding author.
E-mail addresses: ponomarchuk.em14@physics.msu.ru
Full postal address: Leninskie Gory 1 b.2, Moscow 119991 Russia

---

ARTICLE INFO

Keywords:
High intensity focused ultrasound
Non-invasive surgery
Boiling histotripsy
Histology
Computer vision
Neural network

ABSTRACT

This work was focused on the newly developed ultrasonic approach for non-invasive surgery – boiling histotripsy (BH) – recently proposed for mechanical ablation of tissues using pulsed high intensity focused ultrasound (HIFU). The BH lesion is known to depend in size and shape on exposure parameters and mechanical properties, structure and composition of tissue being treated. The aim of this work was to advance the concept of BH dose by investigating quantitative relationships between the parameters of the lesion, pulsing protocols, and targeted tissue properties. A HIFU focus of a 1.5 MHz 256-element array driven by power-enhanced Verasonics system was electronically steered along the grid within 12×4×12 mm volume to produce volumetric lesions in porcine liver (soft, with abundant collagenous structures) and bovine myocardium (stiff, homogenous cellular) *ex vivo* tissues with various pulsing protocols (1–10 ms pulses, 1–15 pulses per point). Quantification of the lesion size and completeness was performed through serial histological sectioning, and a computer vision approach using a combination of manual and automated detection of fully fractionated and residual tissue based on neural network ResNet-18 was developed. Histological sample fixation led to underestimation of BH ablation rate compared to the ultrasound-based estimations, and provided similar qualitative feedback as did gross inspection. This suggests that gross observation may be sufficient for qualitatively evaluating the BH treatment completeness. BH efficiency in liver tissue was shown to be insensitive to the changes in pulsing protocol within the tested parameter range, whereas in bovine myocardium the efficiency increased with either increasing pulse length or number of pulses per point or both. The results imply that one universal mechanical dose metric applicable to an arbitrary tissue type is unlikely to be established. The dose metric as a product of the BH pulse duration and the number of pulses per sonication point (BHD1) was shown to be more relevant for initial planning of fractionation of collagenous tissues. The dose metric as a number of pulses per point (BHD2) is more suitable for the treatment planning of softer targets primarily containing cellular tissue, allowing for significant acceleration of treatment using shorter pulses.

---

1. Introduction

Histotripsy is an emerging technique based on pulsed high intensity focused ultrasound (HIFU) that aims at non-invasive mechanical fractionation of tissue [1–2]. One of the histotripsy types termed boiling histotripsy (BH) utilizes milliseconds-long pulses of HIFU with shock fronts to rapidly achieve the temperature of 100°C in a highly localized region at the focus and thus produce a vapor bubble. The interaction of the remaining shock fronts in the pulse with this vapor bubble leads to disintegration of tissue down to subcellular level through a combination of acoustic atomization, cavitation and microstreaming [3–5]. Potential and currently investigated clinical applications of BH include mechanical ablation of tumors and promoting anti-tumor immune response, disinfection of abscesses, liquefaction of large post-operative or traumatic hematomas, potentiating liquid biopsy and tissue decellularization [1–2, 6–10].

The shape and size of a single histotripsy lesion is known to depend on a combination of HIFU transducer parameters (F-number and frequency, [3, 11–12]), pulsing protocol (pulse duration and shock amplitude at the focus [3, 11–17]), treatment time (number of delivered BH pulses), and on the mechanical properties (stiffness and toughness) of targeted tissue [1, 3, 13–15, 18–19]. It is well established that tissues that are stiff and/or tough, which often implies high collagen content, are more resistant to BH damage, i.e., generally longer treatment, longer pulses and larger pressure amplitudes are required to fully fractionate those tissues, and the resulting lesions are smaller [15, 20–22]. The latter is especially important in volumetric BH ablation, where the focal spot is translated over the targeted volume with a certain spatial step or at a certain speed that has to be optimized to allow individual lesions to merge, yet maximize the ablation speed [17, 23]. Thus, to facilitate BH treatment planning in a given tissue type, it would be helpful to define a quantitative measure of delivered treatment – "BH dose". Such dose concept is well established for thermal therapies, including thermal HIFU, and is used in treatment planning and for real-time feedback on treatment completion [24]. A candidate metric proposed for BH dose was the number of BH pulses delivered per focus location [15], regardless of the pulse duration and shock amplitude, provided that boiling occurs within each pulse. Indeed, in those studies the quality of fractionation within volumetric BH lesions in porcine kidney cortex *in vivo* were similar for the same BH dose, but the dose was quite low (5 pulses per point) and fractionation incomplete. Moreover, the BH outcome was only assessed qualitatively.

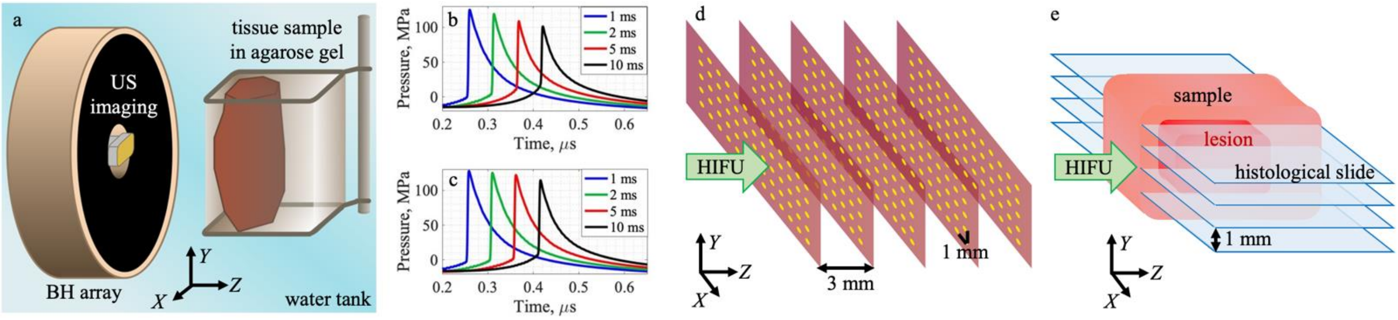

Fig. 1. (a) BH treatment *ex vivo* setup schematics. (b–c) Focal waveforms at the average depth (12 mm) in porcine liver (b) and in bovine myocardium (c) at an average voltage for 1-ms (blue), 2-ms (green), 5-ms (red) and 10-ms (black) pulses. (d) Schematics of sonication geometry for a volumetric treatment. (e) Illustration of lesion histological sectioning allowing for a 3D reconstruction of the lesion volume. In (a, d, e) HIFU was incident from the left.

The goal of this study was to advance the concept of BH dose by quantitatively characterizing the relationships between the parameters of volumetric BH exposures and the size and contents of BH lesions. The lesions were induced in two *ex vivo* tissues with different mechanical properties and composition – bovine myocardium (stiff but very homogenous, cellular tissue) and porcine liver (soft, but includes a large number of collagenous structures of different sizes). Here we proposed and evaluated the following two candidate metrics for the BH dose, which would predict the degree of liquefaction for collagenous and cellular tissues, respectively: a product of the number of BH pulses delivered per sonication point and the BH pulse duration (BHD1, i.e., "total BH time-on"), and the number of pulses per point alone (BHD2). BH treatment outcome for all pulsing protocols and tissue types was evaluated based on three metrics: ablation rate, percentage of total residual tissue within the lesion, and percentage of residual collagenous tissue. Those metrics were estimated from histological slides taken throughout every lesion volume.

To accelerate the process of quantitative histological analysis, a novel computer vision approach was developed here using a ResNet-18 neural network (NN) trained on manually segmented sections. Computer vision approaches have already been successfully developed by others for similar purposes such as classification of different tissue types [25], quantitative assessment of tissue necrosis [26], detection of thermal HIFU lesions [27], cancer detection [28–29], fibrosis identification [30], etc. Mechanically fractionated tissue, however, significantly differs in structure from that subjected to natural or thermal necrosis, and therefore, requires a custom-developed neural network approach for fast and accurate automated lesion segmentation.

2. Materials and Methods

2.1. Tissue sample preparation

Volumetric BH ablations were performed in two *ex vivo* tissues – porcine liver and bovine myocardium – collected either from unrelated *in vivo* animal studies ongoing on-site or from a local abattoir, respectively. The tissue samples were kept refrigerated in isotonic saline for less than 48 hours after harvesting prior to the experiments, then degassed for at least 1 hour in a desiccant chamber at -690 Torr, and embedded into a low melting point agarose gel (UltraPure Agarose; Invitrogen) for ease of positioning (Fig. 1a). Porcine liver samples were embedded in such an orientation that they were sonicated through liver capsule.

2.2. BH apparatus and pulsing parameters

The BH exposures were performed using a 1.5 MHz 256-element HIFU array (outer diameter 14 cm, *F*-number 0.83) described in detail elsewhere [23] driven by Verasonics Ultrasound Engine V1 system in a tank filled with de-ionized de-gassed water (Fig. 1a). Targeting and treatment monitoring in real time were performed using an ultrasound (US) imaging probe (3PE, Humanscan, Gyeonggi-do, South Korea) incorporated into the central opening of the array. The following BH exposure parameters were varied (Table 1): BH pulse duration (within the range of 1–10 ms) and number of pulses per sonication point – N_p (within the range of 5–15) referred to here as *ppp* (pulses per point) for brevity. Duty cycle was kept at 1%, therefore pulse repetition frequency (PRF) was adjusted for each pulse duration

Table 1
Exposure parameters for volumetric BH treatments

Tissue	Pulse length	PRF	N_p	Acoustic output power	Focal P^+ / P^- / A_s *in situ*	t_b
Porcine liver	1 ms	10 Hz	5	457 W	125.1 / -17.7 / 125.7 MPa	0.86 ms
			10			
			15			
	2 ms	5 Hz	15	368 W	119.1 / -16.6 / 115.6 MPa	1.1 ms
			10			
			5			
	5 ms	2 Hz	15	284 W	108.7 / -15.2 / 98.6 MPa	1.78 ms
			10			
			5			
	10 ms	1 Hz	15	251 W	101.2 / -14.5 / 87.1 MPa	2.58 ms
			10			
			5			
Bovine myocardium	1 ms	10 Hz	15	508 W	127.7 / -18.3 / 130.5 MPa	0.85 ms
			10			
	2 ms	5 Hz	10	457 W	125.1 / -17.7 / 125.7 MPa	0.95 ms
			5			
	5 ms	2 Hz	5	410 W	121.9 / -17.1 / 120.7 MPa	1.07 ms
			10			
	10 ms	1 Hz	5	323 W	114.4 / -15.9 / 107.9 MPa	1.5 ms
			10			

PRF = pulse repetition frequency; N_p = number of pulses per sonication point; P^+ (P^-) = peak positive (negative) focal pressure at the average depth (12 mm) *in situ*; A_s = focal shock amplitude at the average depth (12 mm) *in situ*; t_b = time to reach boiling at the average depth (12 mm) *in situ*.

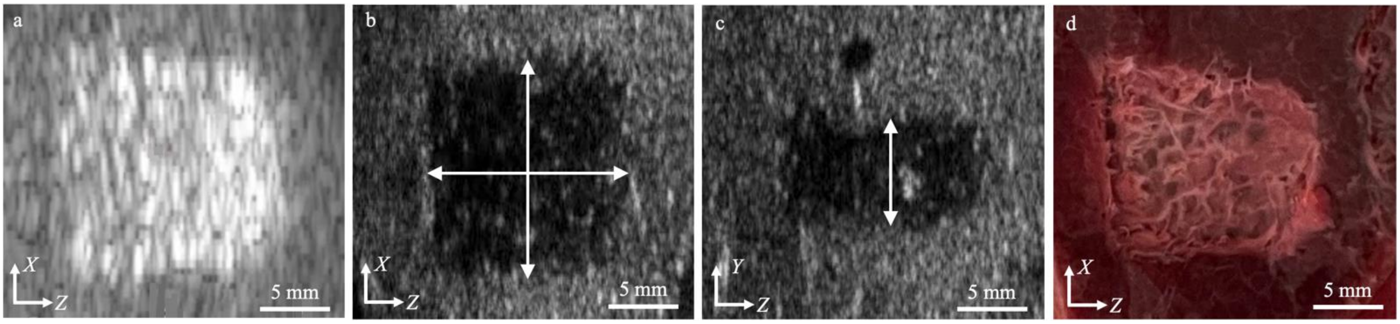

Fig. 2. Example of a lesion gross observation (HIFU incident from the left). (a) B-mode image of the lesion immediately after the treatment obtained with the US probe integrated with HIFU transducer. (b–c) High resolution B-mode images of the lesion taken 30 min post-treatment by a separate probe and corresponding measurements of the lesion dimensions along the *X* and *Z* (b), and *Y* axis (c). (d) Gross image of the lesion bisected in the axial *XZ* plane and filled with saline. Scale bar is 5 mm for all images.

within 1–10 Hz. Prior to each BH ablation, a threshold DC voltage was defined for each sample by delivering individual BH pulses to the nominal focus of the array while increasing the DC voltage until a bright hyperechoic spot was observed on the B-mode US imaging at the focus indicating bubble formation. The sonication then was performed at a voltage exceeding the defined threshold by 10%.

The *in situ* focal pressure waveforms corresponding to each BH exposure (Fig. 1b–c) were obtained from numerical simulations of the nonlinear acoustic field described by Bawiec et al (2021) [23], and nonlinear derating procedure [31–32]. The tissue attenuation coefficients at 1.5 MHz required for derating were taken from [15, 33] and were α = 0.052 Np/cm for porcine liver tissue and α = 0.094 Np/cm for bovine myocardium tissue. The resulting peak focal pressures *in situ* are given in Table 1 and the shock amplitude was used to estimate the time to reach boiling as $t_{\mathrm{b}} = \frac{\Delta T c_V 6\rho^2 c^4}{\beta f_0 A_S^3}$ to verify that boiling would be induced within each pulse [32]. Here ΔT is the temperature change from the ambient to the boiling temperature of 100°C, c_{v} is the tissue heat capacity per unit volume, ρ is the tissue density, c is its sound speed, β is the tissue nonlinear parameter, f_0 is the ultrasound frequency, and A_{s} is the shock amplitude at the focus *in situ*. The tissue properties required for time-to-boil estimations were taken from the literature [13, 33–35] and were as follows: $\rho = 1070\ \mathrm{kg \cdot m^{-3}}$, $c = 1588\ \mathrm{m \cdot s^{-1}}$, $\beta = 4.5$, $c_{\mathrm{v}} = 3.66\ \mathrm{MJ \cdot m^{-3} \cdot K^{-1}}$ for porcine liver tissue; and $\rho = 1060\ \mathrm{kg \cdot m^{-3}}$, $c_0 = 1570\ \mathrm{m \cdot s^{-1}}$, $\beta = 4.1$, $c_{\mathrm{v}} = 3.94\ \mathrm{MJ \cdot m^{-3} \cdot K^{-1}}$ for bovine myocardium tissue.

N = 2–4 lesions were produced using each pulsing protocol. The targeted volume in each tissue sample was liquefied by consecutively ablating 5 planes orthogonal to the beam axis with a 3 mm step, starting from the plane distal from the source (Fig. 1d). In each plane, a grid of 13×5 points with 1 mm step was sonicated N_{p} times with a random order of sonication points within each 13-point row, starting from the central row and then alternating sides and moving away from the beam axis in the elevational dimension. The HIFU focus was electronically steered over the treatment grid. The overall treatment time for the full grid (12×4×12 mm, volume 0.576 ml) was 2.7–81 minutes depending on the pulsing protocol. The obtained lesions were visualized and measured 30 min post-treatment with L14-5 linear probe (Sonix RP, Ultrasonix Medical Corporation, Canada) inside the water tank prior to any manipulations (Fig. 2b–c). The resulting ablated volume depended on the pulsing protocol and tissue type and was estimated either from the ultrasound images as a product of the three measured dimensions (Fig. 2) or from histological analysis (see below). One lesion per protocol was further used for histological analysis, and the other 1–3 lesions per protocol were bisected along the imaging plane, rinsed with saline and analyzed grossly (Fig. 2d).

2.3. Quantitative histological analysis

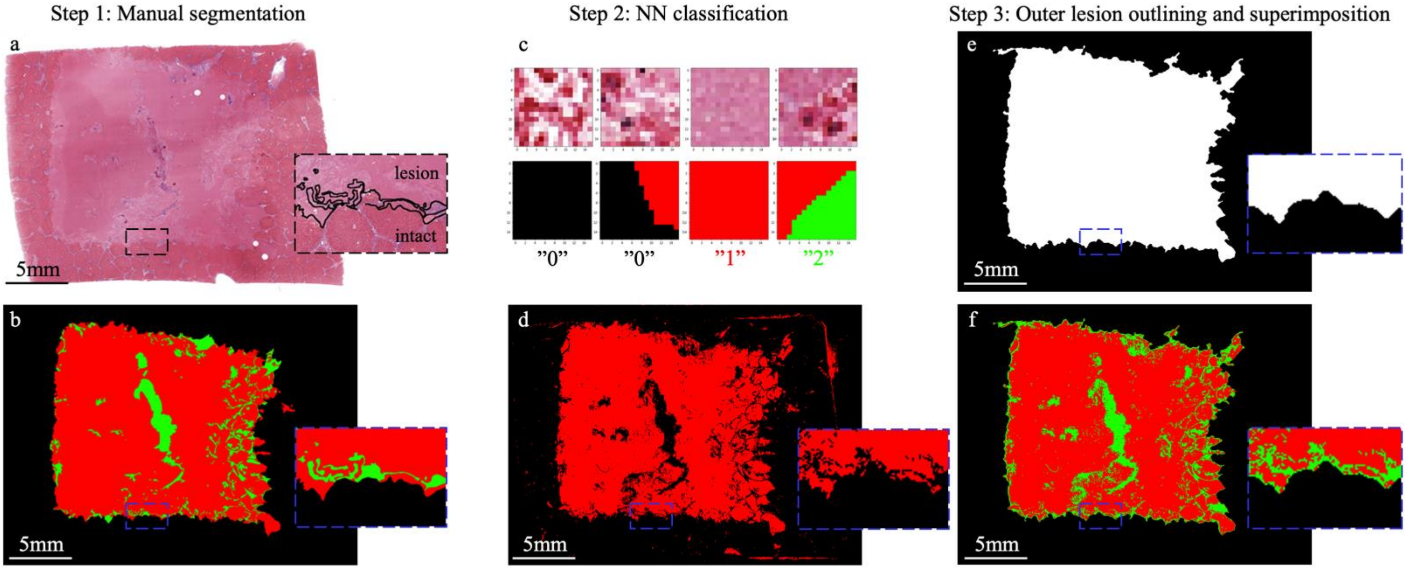

Fig. 3. Illustration of the steps of quantitative histological analysis of BH lesions in porcine liver tissue (HIFU incident from the left). (a) MT-stained histological section taken in the center of the lesion. Dashed box shows a magnified part near the lesion border with a black line indicating manually defined outline of the lesion. (b) Resulting mask of manual three-class segmentation: red = fully fractionated tissue, green = intact or partially damaged tissue remaining within the lesion, black = background and intact tissue outside the lesion. (c) Example dataset of the 40×40 µm tiles with the assigned class numbers for NN classification: "0" – background and intact tissue outside the lesion; "1" – fully fractionated tissue; "2" – residual tissue within the lesion. (d) Resulting mask of fully fractionated tissue after NN classification after combining classes "0" and "2" before post-processing. (e) Resulting mask of the lesion interior (including both fully fractionated and residual tissue) after post-processing. (f) Final three-class NN mask after post-processing, to be compared to (b). Dashed boxes in (a–b, d–f) show the same border part of the lesion magnified. Scale bars in (a–b, d–f) are 5 mm.

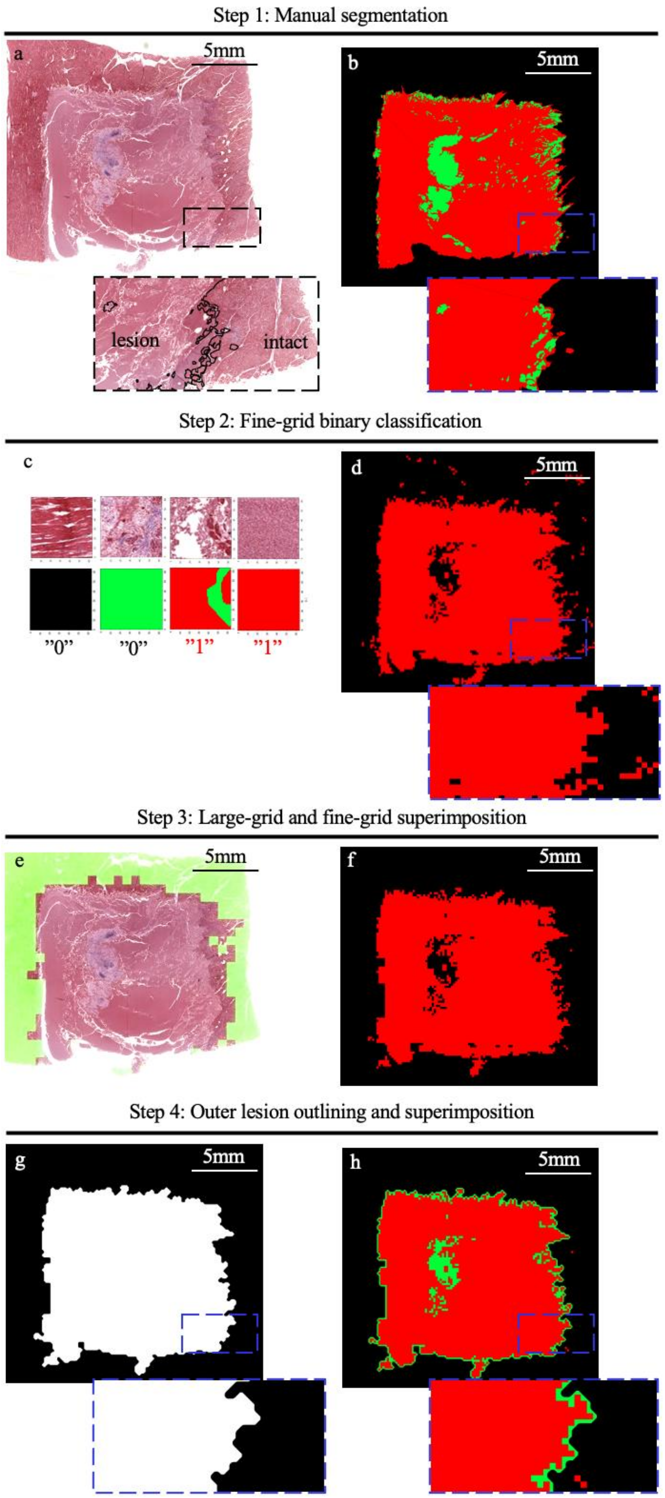

Fig. 4. Illustration of the steps of quantitative histological analysis of BH lesions in bovine myocardium tissue (HIFU incident from the left). (a) MT-stained histological section taken in the center of the lesion. Dashed box shows a magnified part near the lesion border with a black line indicating manually defined outline of the lesion. (b) Resulting mask of manual three-class segmentation: red = fully fractionated tissue, green = intact or partially damaged tissue remaining within the lesion, black = background and intact tissue outside the lesion. (c) Example fine-grid dataset of the 160×160 μm tiles with the assigned class numbers for binary NN classification: "0" – background, intact and residual tissue; "1" – fully fractionated tissue. (d) Resulting mask of fully fractionated tissue after fine-grid (160×160 μm) binary NN classification before post-processing. (e) Large-grid mask (644×644 μm) of intact tissue after binary NN classification superimposed onto histological section (a). (f) Resulting mask after fine-grid and large-grid masks superposition before post-processing. (g) Resulting mask of the lesion interior (including both fully fractionated and residual tissue) after post-processing. (h) Final three-class NN mask after post-processing, to be compared to (b). Dashed boxes in (a–b, d, g–h) show the same border part of the lesion magnified. Scale bars in (a–b, d–h) are 5 mm.

For each BH pulsing protocol one of the lesions was fixed in formalin *en bloc*, embedded in paraffin, then 5-μm histological sections were taken through the entirety of each lesion with a 1 mm step (Fig. 1e) and stained with Masson's Trichrome (MT) stain. The stained sections were digitized at 4X magnification and their analysis was performed using a combination of manual and computerized segmentation using a convolutional 18-level neural network ResNet-18 [36] that has been successfully applied in numerous medical tasks [37].

Lesion analysis in porcine liver

Steps of the quantitative analysis of the volumetric lesions are illustrated in Fig. 3 on a representative histological section of a BH lesion in liver tissue. First, histological sections of BH lesions in liver tissue with the highest (10 ms, 10 ppp) and the lowest (1 ms, 5 ppp) exposure doses were manually segmented using open-source computer vision annotation tool (cvat.org) to outline fully fractionated tissue (red in Fig. 3b), intact or partially damaged tissue within the lesion (green in Fig. 3b), and background or intact tissue outside the lesion (black in Fig. 3b). Four of the manually analyzed images were then divided into a lattice of square tiles approximately 40×40 μm each (16×16 pixels). Each tile was classified either as class "1" (fully fractionated tissue – red), class "2" (residual tissue within the lesion – green), or as class "0" (background or intact tissue outside the lesion – black) if the area of the corresponding color from manual segmentation exceeded 55% of the tile area (Fig. 3c). Remaining unclassified tiles were not included in the dataset. The dataset for neural network training was then compiled from 100 000 tiles of class "0", 100 000 tiles of class "1" and 34 000 tiles of class "2". The dataset was randomly split into the Train and Test sets, consisting of 80% and 20% of the segmented data, respectively. The neural network (NN) Resnet-18 was trained on this dataset, and the final classification accuracy reached 97%. The final training parameters were as follows: batch size was 20000 fragments, learning rate was 0.002, number of epochs was 120; the Adam optimizer was used, and CrossEntropyLoss was selected as the loss function. Since the intact tissue (green in Fig. 3b) within the lesion was not distinguishable from the intact tissue outside the lesion (black in Fig. 3b), the classes "0" and "2" were then combined (Fig. 3d). Therefore, resulting NN masks (Fig. 3d) were two-colored: red for fully fractionated tissue, black for everything else. To eliminate the intercellular space that may be confused with fractionated tissue at a high magnification, isolated single red tiles were removed by the neural network. Some defects of histological slides, such as section cuts and folds, air bubbles, or staining defects, were manually corrected in the NN masks.

The NN masks (Fig. 3d) were then post-processed using open-access Computer Vision libraries of MATLAB and Python to define the continuous outer lesion outline including fully fractionated and residual tissue (Fig.3e). For that, contours of all clusters in NN masks (Fig. 3d) were defined and, first, dilated to an optimal distance that was defined empirically for each tissue type to merge the neighboring clusters together. Then the remaining holes were filled in and the clusters were eroded back by the optimal distance used earlier for their dilation. Then all resulting clusters not exceeding 80% of the largest cluster area were removed to preserve only lesion-containing clusters and eliminate small vessels and intercellular space outside the lesion typically incorrectly classified as fully fractionated tissue. Finally, superimposition of the lesion interior masks (Fig. 3e) and NN masks (Fig. 3d) for each section resulted in a three-class segmentation result (Fig. 3f). This allowed for NN accuracy validation by comparison with manually segmented images to adjust the parameters of dataset or neural network training, if needed.

Once the sufficient accuracy was achieved (errors within 3% of the analyzed image) by adjustment of the dataset and training parameters and post-processing procedure, the network was applied to the remaining histological sections using the same steps described above. Note that morphological operations, i.e., dilation and erosion, applied to NN masks during their post-processing led to a slight overestimation of the lesion area and, therefore, erroneous appearance of a one-tile thick lesion contour (Fig. 3f, Fig. 4h). The introduced error, however, was within 3% of the image area and, therefore, was within our accuracy threshold.

Each lesion volume was then calculated from the collection of 2D images by integration along the dimension perpendicular to the sections: the obtained lesion areas in every histological section were multiplied by the 1-mm step for the internal sections and by 0.5 mm for the boundary sections, and then summed to obtain the corresponding lesion volume. The ablation rate was then estimated as a ratio of the lesion interior volume and the treatment time in each parameter set.

Another BH exposure metric, apart from ablation rate, was the area percentage of residual (i.e., intact or partially damaged) tissue within the lesion. Each lesion was averaged over its consecutive histological sections; only those sections that contained over 50% area of the largest lesion cross-section were considered.

Lesion analysis in bovine myocardium

For lesions produced in bovine myocardium tissue, analysis was performed by binary classification of larger 160×160 μm tiles (64×64 pixels) due to the difference in cellular structure *vs* that in liver (Fig. 4). Each tile was classified either as class “1” (fully fractionated tissue – red) if the red color area from manual segmentation exceeded 55% of the tile, or as class “0” for the rest of the tiles. The dataset consisted of 23 000 tiles of each class, “0” and “1”, and was split into the Train and Test sets at a ratio of 80% : 20% of the dataset. The Resnet-18 was then trained on this dataset for binary classification task, and the final accuracy reached 93%. The final training parameters were as follows: batch size was 2000 fragments, learning rate was 0.0002, number of epochs was 130; the Adam optimizer was used, and CrossEntropyLoss was selected as the loss function. However, the fibrillar structure of cardiac tissue led to intercellular space between muscle fibers being incorrectly classified as fractionated tissue by a fine-grid NN segmentation. Such regions were often located in close proximity to the lesion (Fig. 4d) and could erroneously enlarge the lesion area during dilation in post-processing. To eliminate such regions from fine-grid NN masks, the network was also trained on larger 644×644 μm (256×256 pixels) tiles to detect intact tissue areas alone (Fig. 4e). These areas were then superimposed onto the results of a fine-grid segmentation (Fig. 4d) to derive the NN masks (Fig. 4f) used for subsequent post-processing and accuracy validation (Fig. 4g–h).

Collagenous tissue analysis

The third metric of BH exposure outcome considered here was the percentage of residual collagenous tissue. Collagenous tissue structures were segmented by applying color and spatial filtering and binary image processing tools of an open-source software (Fiji, NIH, Bethesda, MD) to MT-stained histological sections. Color filtering was performed in HSB (hue-saturation-brightness) color space. To extract tissue from the slide background, a brightness filter with 0–200 limits was applied and the holes were then filled in. Then the extracted tissue was separated into the lesion and surrounding tissue (Fig. 5a) by superimposing the NN masks such as Fig. 3e or Fig. 4g onto the histological image. Within the extracted lesion or surrounding tissue, the collagenous tissue was detected by applying color and spatial filters (Fig. 5b). The color filter limits were defined by analyzing the HSB distributions of manually cropped images of collagenous tissue and were as follows: [165–227; 0–255; 0–233] for porcine liver and [150–227; 0–255; 0–170] for bovine myocardium tissue. The spatial filter was applied to eliminate the cell nuclei that had similar color to collagenous tissue when stained by MT. The spatial filter lower limit was determined by manual sizing of the smallest visible cell nuclei in both tissue types and was found to be 95 μm^2 (15 px^2) for both liver and myocardium tissue. This implied the cell nuclei had to look like 9.7×9.7 μm squares which agrees with the results for cell diameter around 6.5 μm published in [38–39] considering limitations of the digitization resolution used in this study. The percentage of collagenous tissue area both inside and outside the lesion was then estimated. To evaluate the reduction of collagenous tissue by BH exposure, the percentage of collagenous tissue within the lesion was divided by that outside the lesion. The resulting value was considered the third BH outcome metric and is further referred to as the percentage of residual collagenous tissue. To estimate this ratio in porcine liver, collagenous tissue percentage outside the lesion was considered for each section separately. Cardiac tissue, however, had fewer and less evenly distributed collagen-containing structures; therefore, collagenous tissue percentage outside the lesion was averaged over all available myocardium sections, including those devoid of any lesions. The estimated ratios were then averaged for each volumetric lesion over the sections considered in residual tissue estimation.

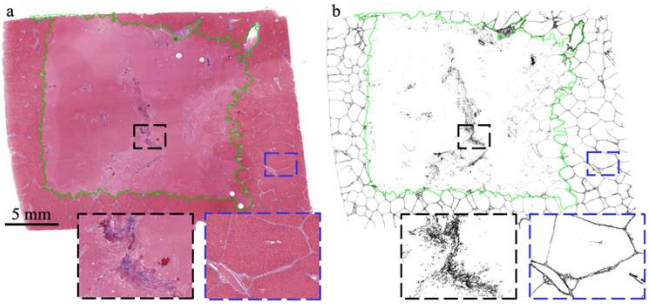

Fig. 5. Illustration of collagenous tissue detection process on the example of porcine liver section (HIFU from the left). (a) MT-stained section with a green line indicating lesion outline derived from a lesion interior mask Fig. 3e. (b) Result of collagenous tissue detection in image (a). Dashed boxes show magnified parts of the lesion (black) and intact tissue outside the lesion (blue). Scale bar is 5 mm for both images.

Statistical analysis

A two-tailed two-sample homoscedastic Student’s t-test was performed to compare the following BH outcome metrics between different treatments: the percentage of total residual tissue and the percentage of residual collagenous tissue. Significance threshold was set at $p = 0.05$.

3. Results

3.1. Validation of neural network algorithm accuracy

All values of lesion interior area and fully fractionated tissue area predicted by a combination of NN approach and post-processing were within a 3% margin of the area analyzed manually (Fig. 6). Therefore, all results derived from histology and described further were obtained from the NN algorithm. This figure is also illustrative of the range of the lesion area that could be encountered in consecutive histological sections of a single lesion.

3.2. Ablation rate calculation

Fig. 7 summarizes the dependence of the lesion volumes and corresponding ablation rates on the BH exposure parameters in porcine liver (a–b) and bovine myocardium (c–d) tissues. Empty bars correspond to the lesion volumes derived from US imaging, filled bars – to those derived from 3D reconstruction of the histological sections. As seen in Fig. 7a, lesion volumes derived from histology are typically up to 40–50% lower than those estimated from US images due to a known shrinkage effect of formalin-fixed

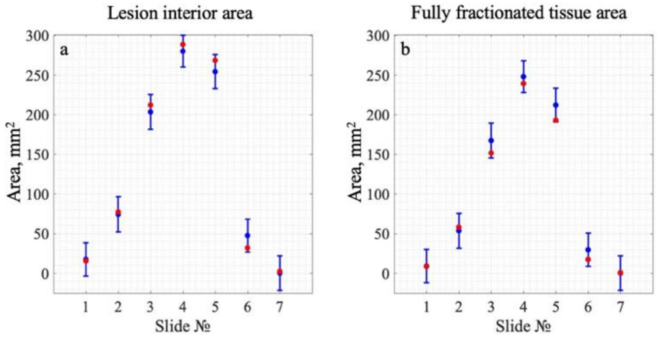

Fig. 6. Manual (blue) and neural network (red) resulting area estimations for all slides throughout one of the lesions produced in porcine liver tissue with the highest exposure parameters (10 ms, 10 ppp): (a) – lesion interior areas (i.e., including fully fractionated tissue and residual tissue inside the lesion); (b) – fully fractionated tissue areas. Blue error bars indicate the targeted error margin of 3% from each analyzed histological image.

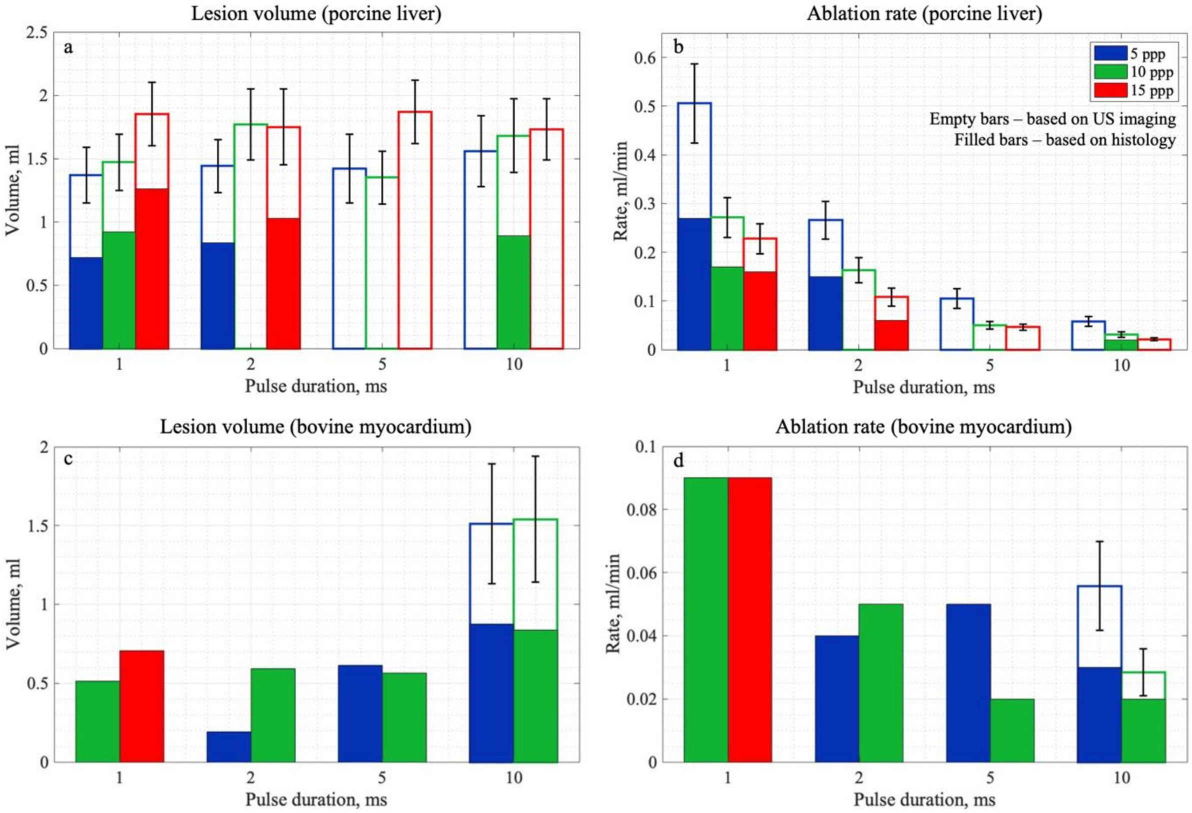

Fig. 7. Lesion volumes (a, c) and corresponding ablation rates estimated from 3D reconstruction of histological sections (filled bars) or from ultrasound images (empty bars) obtained using varied pulse durations and number of pulses per sonication point (ppp): 5 ppp (blue), 10 ppp (green) and 15 ppp (red) in porcine liver tissue (upper row) and bovine myocardium tissue (bottom row). Note that histology-based values shown here are underestimated due to histological sample shrinkage effect during formalin fixation. Error bars represent indirect volume measurement errors of the US imaging.

histological specimens [40]. The overall trend, however, remains, allowing for comparative analysis across the exposure parameters.

In porcine liver tissue (Fig. 7a) at the largest pulse duration (10 ms), the liquefied volume was not affected by the number of pulses per point (ppp) within the considered range of 15 to 5 ppp within measurement error. With the decrease in pulse length, the difference in ablated volume between varied ppp became more noticeable. Due to the proportionally higher PRF, the use of shorter pulses and lower ppp resulted in substantially higher ablation rates (Fig. 7b).

In cardiac tissue, similarly to liver, histology-based volumes of the lesions were 40–50% lower than those estimated from ultrasound images. The lesions were also smaller and less complete (Fig. 7c) than those produced in liver tissue using the same exposure parameters. For example, delivering 2-ms pulses with 5 ppp was shown to be insufficient for the grid of individual lesions to effectively merge in cardiac tissue (Fig. 7c), whereas even shorter 1-ms pulses with 5 ppp were sufficient for uniform liquefaction of liver tissue (Fig. 7a). At increasing pulse lengths and ppp, the liquefied volume increased, reaching saturation (i.e., independence from the ppp) at longer pulses (5 and 10 ms). The use of shorter pulses and lower ppp, however, allowed for treatment acceleration (Fig. 7d), similarly to what was observed in liver tissue.

3.3. *Residual tissue percentage estimation*

Fig. 8 demonstrates the results for estimation of total (Fig. 8a,c) and collagenous (Fig. 8b,d) residual tissue percentage as metrics of BH exposure outcome. The mean values of total residual tissue percentage (dashed lines in Fig. 8a,c) were 27% and 18% for liver and myocardium tissue, respectively, which was lower than percentage of residual collagenous tissue – 33% and 53%, respectively (dashed lines in Fig. 8b,d). This quantitatively corroborates prior findings that collagenous structures are more resistant to BH than cellular structures [15, 18]. Porcine liver tissues appeared to be insensitive to the changes in BH exposure parameters within the tested range (Fig. 8a–b) as Student's t-test revealed no statistically significant difference (at $p < 0.05$ level) in percentage of total or collagenous residual tissue for any exposure conditions. In bovine myocardium, however, BH treatment outcomes differed more noticeably for different pulsing schemes (Fig. 8c–d). The use of longer pulses and/or higher ppp resulted in lower percentage of total and collagenous residual tissue after the myocardium treatment, with (1 ms, 15 ppp) and (10 ms, 10 ppp) parameter sets resulting in statistically the same tissue fractionation outcome.

The structure of residual tissue, however, was noticeably different after the treatment with the same number of BH pulses per point but with shorter *vs* longer ultrasound pulses (Fig. 9). For collagenous tissue, the use of short pulses (1–2 ms) resulted in fine tissue structures remaining within the lesion volume such as lobule walls seen in liver tissue (Fig. 9b–d). The post-treatment B-mode images correspondingly showed residual echogenic structures within the lesions (Fig. 9a, Fig. 10a). Treatment with longer pulses (5–10 ms) even with lower ppp than with shorter pulses typically destroyed fine-scale tissue structures and left either liquid-filled void with residual tissue located mainly at the lesion border (Fig. 9e–f) or larger tissue structures such as those illustrated in Fig. 9g–h and Fig. 10f–h. The B-mode images after treatment with longer pulses showed more homogeneous and more hypoechogenic lesions (Fig. 9e, Fig. 10e) as compared to those produced by shorter pulses (Fig. 9a, Fig. 10a). None of the protocols with short 1–2 ms pulses within the tested range of 5–15 ppp were able to

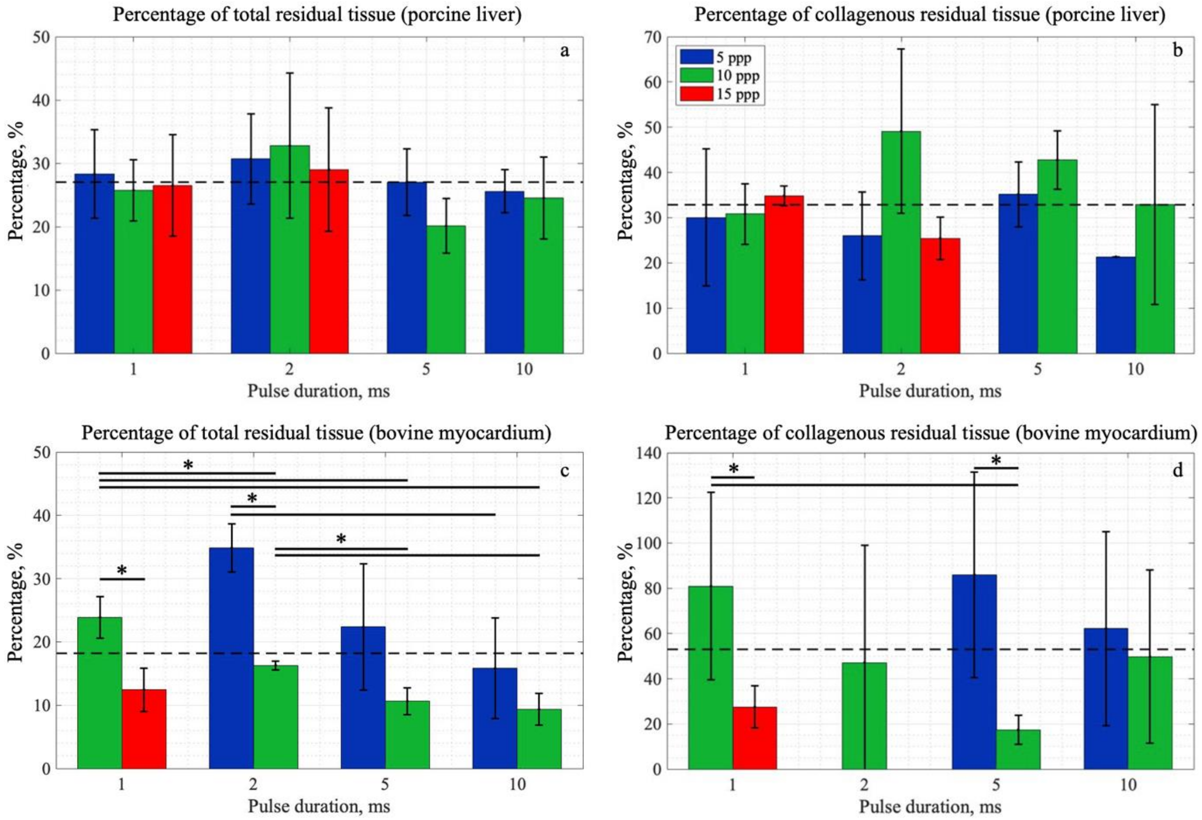

Fig. 8. Average percentage of total residual tissue (a,c) and collagenous residual tissue (b,d) for varied pulse durations and number of pulses per sonication point (ppp): 5 ppp (blue), 10 ppp (green) and 15 ppp (red) in porcine liver tissue (upper row) and bovine myocardium tissue (bottom row). Data represents mean values; error bars represent standard deviations, * represents statistical significance at $p < 0.05$. Dashed line in each graph corresponds to the average value over all bars of the graph. Note that (2 ms, 5 ppp) set was insufficient for individual lesions to merge and, therefore, was not analyzed for collagenous tissue.

completely fractionate the collagenous lobule walls in liver tissue. For longer pulses (5–10 ms), the minimum required for that was 10 ppp with 5-ms pulses, and 5 ppp with 10-ms pulses. This agrees with the concept of BHD1 metric – a product of the pulse duration and the number of pulses per point. Conversely, in the predominantly cellular cardiac tissue and cellular component of liver tissue, the lesion completeness was primarily determined by BHD2 metric – the number of pulses per point, regardless of their duration. For instance, the twofold decrease in BH pulse duration (from 10 ms to 5 ms) resulted in similar lesion completeness in myocardium with BHD2 = 10 ppp, and the tenfold decrease in pulse duration (from 10 ms to 1 ms) required only 1.5 times increase in ppp to achieve the same degree of tissue fractionation (Fig. 8c,d). However, the BHD2 threshold for complete

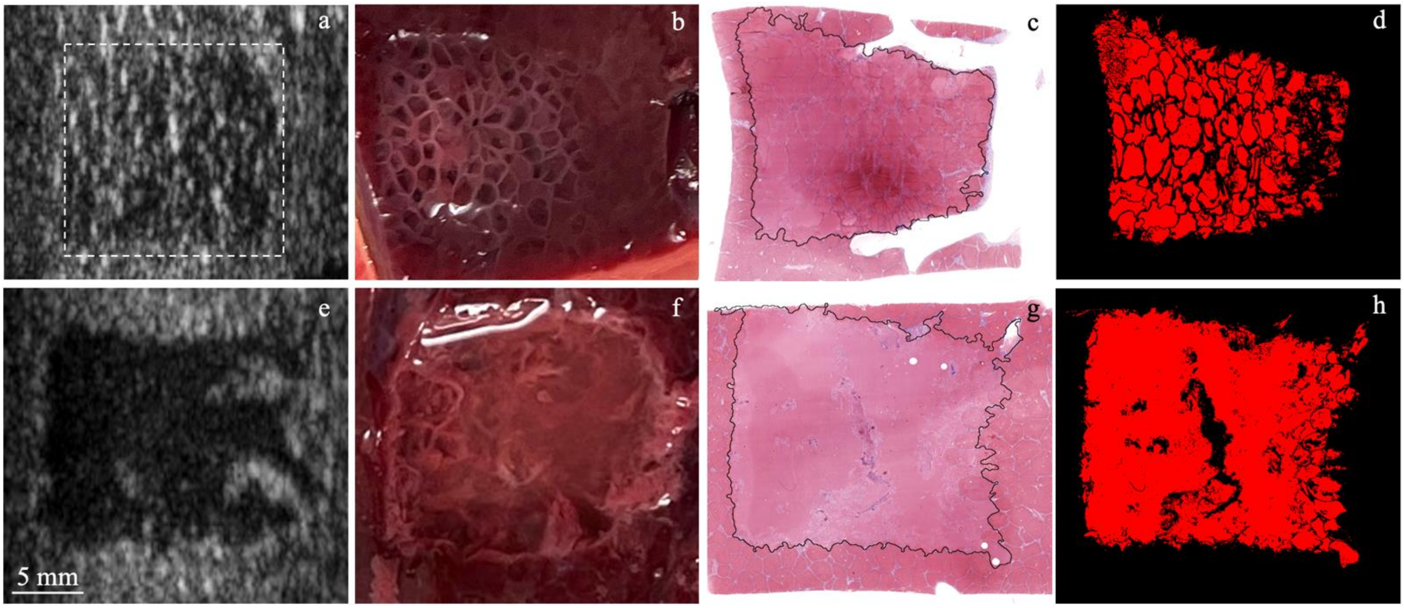

Fig. 9. Illustration of different structure of residual tissue after liver treatment with shorter (a–d) *vs* longer (e–h) ultrasound pulses (HIFU incident from the left). (a,e) B-mode images of the lesions taken 30 min after the treatment (L14-5 Sonix RP probe). Dashed line in (a) outlines the lesion. (b,f) Gross images of the lesions bisected in the axial *XZ* plane and filled with saline. (c,g) MT-stained histological sections of the lesions with black contour of the lesion derived from NN approach after post-processing. (d,h) Masks for fully fractioned tissue (red) of the lesions c,g. Scale bar is 5 mm for all images.

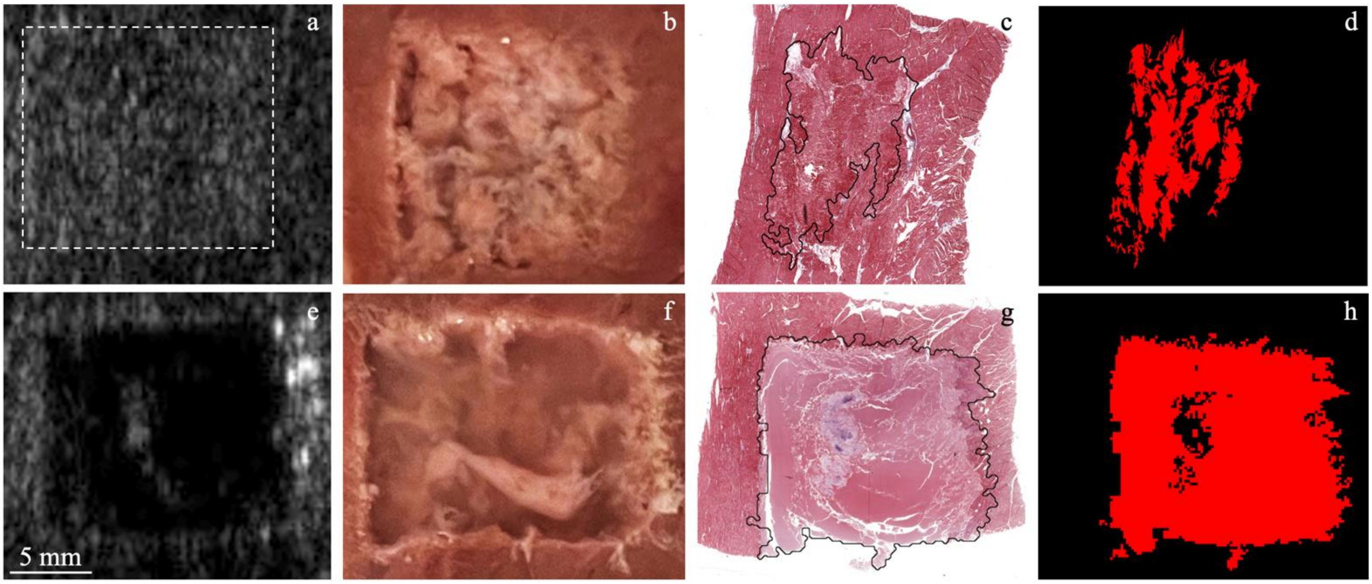

Fig. 10. Illustration of the lesions produced in bovine myocardium with insufficient (a–d) and sufficient (e–h) exposure parameters (HIFU incident from the left). (a,e) B-mode images of the lesions taken 10 min after the treatment (L14-5 Sonix RP probe). Dashed box in (a) outlines the lesion. (b,f) Gross images of the lesions bisected in the axial *XZ* plane and filled with saline. (c,g) MT-stained histological sections of the lesions with black contour of the lesion derived from NN approach after post-processing. (d,h) Masks for fully fractioned tissue (red) of the lesions c,g. Scale bar is 5 mm for all images.

liquefaction of different cellular tissues was found to be different, with the cardiac tissue being more resistant to BH than cellular component of the liver tissue. Specifically, some of the lower dose pulsing protocols were insufficient for the grid of lesions to effectively merge in bovine myocardium tissue (Fig. 10b–d), whereas all parameter sets resulted in volumetric lesion formation in liver tissue samples.

4. Discussion

The goal of this study was to investigate quantitative relationships between the outcomes of BH volumetric tissue liquefaction and exposure parameters (pulse length and number of pulses per point – ppp) for different types of targeted tissue, towards the development of the BH dose metric. Treatment outcome was quantified by the ablation rate and the degree of tissue fragmentation based on percentage of total residual tissue and residual collagenous tissue within the lesion.

For both *ex vivo* porcine liver and bovine myocardium tissues, the use of shorter pulses and/or lower ppp resulted in higher ablation rate but left fine-scale tissue structures (mainly collagenous tissue, such as lobule walls) remaining inside the lesion volume. These findings are in agreement with the results in [6, 15, 18] reporting on the ability of short (microsecond-long) histotripsy pulses erode smaller tissue fragments as compared to longer (millisecond-long) pulses. However, both long and short pulses, given sufficient number of pulses per point, were able to produce lesions with statistically similar degrees of tissue fractionation as indicated by the total and collagenous residual tissue percentage. For both tissue types, the mean values of total and collagenous residual tissue percentage were less than 100% indicating the tissue was indeed fractionated by the treatment. The average values for total residual tissue percentage regardless of tissue type were lower than that for collagenous tissue alone. This indicated higher resistance of collagenous tissue to BH fractionation as compared to other tissues, and agrees with literature [15, 18].

The structure of collagenous residual tissue, however, significantly depended on the BH pulse duration used. In collagenous content of liver tissue, 5 ms 10 ppp and 10 ms 5 ppp protocols (i.e., BHD1 = 50 ms) were able to fractionate the collagenous lobule walls, while none of the protocols with 1–2 ms pulses within the tested range of 5–15 ppp (i.e., BHD1 = 5–30 ms) were sufficient to achieve that. These results indicate that, for collagenous tissues, the BHD1 dose metric – a product of the BH pulse duration and the number of pulses per sonication point – may be more suitable than the number of pulses per point alone. In mostly cellular cardiac tissue and cellular component of liver tissue, however, nearly the same ppp, i.e., BHD2, was required to achieve similar degree of tissue fractionation with varied pulse duration. This indicates that for cellular tissues the number of pulses per sonication point alone may be a more suitable BH dose metric. These results imply that the ablation rate of tissues low in collagen may be significantly increased by the use of shorter pulses. Acceleration of the treatment of collagenous tissues can also be achieved with shorter BH pulses as was shown in [20] but is more limited than in cellular tissues, and the BHD1 metric is meant to serve as a benchmark for the pre-treatment planning in tissues abundant with collagenous structures.

A number of BH mechanical dose metrics could potentially be introduced due to a wide range of sensitivity to BH in different tissues, as opposed to common sensitivity to thermal ablation. This calls in question the possibility to establish a universal BH dose applicable to any tissue type. However, within the pulsing protocol parameter space established for successful BH [12–13, 15, 18, 41] only two parameters remain variable – the BH pulse duration and the number of pulses per sonication point, given that boiling is induced within each pulse. Therefore, the two following candidate metrics for mechanical BH dose were proposed and evaluated here: the product of the number of pulses and pulse duration (BHD1, i.e., “total BH time-on”) and the number of pulses per sonication point (BHD2). It was shown that BHD1 is most suitable candidate metric for collagenous tissues, whereas BHD2 is more applicable for cellular tissues low in collagen.

An important outcome of this study was the development of a novel algorithm allowing for faster quantitative histological analysis using neural network approach as compared to manual outlining. This approach, however, has its limitations such as classification errors of the neural network that required meticulous manual correction. Such inaccuracies were mainly present in challenging histological sections, e.g., containing cuts, folds, air bubbles, staining defects, etc., and arguably could be amended by further refinement of the appropriate dataset and network training parameters. One limitation of the study was a possible interpolation error during 3D reconstruction of lesion volumes from 2D histological sections. This may have had most impact on estimations of residual fragments as their sizes were typically less than the step between sections. To avoid this mistake, here we estimated the percentage of residual tissue in each section individually and then averaged the values.

Of note, tissues are known to shrink during formalin fixation for histology [40], which was observed in the present study as well. Therefore, treated volumes and ablation rates estimated from histology in this work were underestimated. The relative comparisons are still relevant, but it should be taken into account that the actual ablation rates were almost twice as high. Moreover, good agreement between gross images of bisected lesions and histological images of the lesions produced with the same exposure parameters observed in this study (Fig. 9–10) suggests that gross inspection can be used for qualitative estimation of optimal treatment parameters instead of the use of rather costly and time-consuming histological analysis.

Overall, our findings imply that a universal mechanical dose of BH applicable for any tissue type may not be established since tissues with different mechanical properties and composition respond differently to mechanical fractionation as opposed to thermal damage. Therefore, a real-time quantitative metric of the BH treatment completion, such as, for example, a currently developing color Doppler technique [42], would be a critical option for future clinical use. However, the results obtained here and the two candidate dose metrics can be used as benchmarks for initial pre-treatment planning. In particular, fractionation of collagenous tissues could be planned based on the BHD1 metric, a product of the BH pulse duration and the number of pulses per sonication point, given the boiling is induced within each pulse. In that context, the threshold BHD1 = 50 ms would correspond to complete liquefaction of collagenous components in liver. If a primary target tissue is mostly cellular, similarly to myocardium, the treatment could be planned based on the threshold BHD2, a number of pulses per sonication point. For example, BHD2 = 10 ppp should be sufficient to liquefy myocardium tissue.

5. Conclusions

This work was aimed towards the development of mechanical dose metrics that would characterize successful BH ablation of various types of tissues using pulses of various length. Relationships between treatment outcome and exposure parameters were quantified for porcine liver and bovine myocardium tissues *ex vivo*. The results showed that both longer and shorter BH pulses were capable of producing well-demarcated lesions with statistically similar tissue fractionation degree given sufficient number of pulses per sonication point had been applied. However, tissue stiffness, composition, and structure all influence the tissue response to the same BH exposure parameters. This implies that one universal mechanical dose metric applicable to an arbitrary tissue type is unlikely to be established. Here, two dose metrics were proposed and evaluated. It was shown that the treatment of mostly cellular tissues can be initially planned based on the BHD2 metric – a number of pulses per sonication point. This allows the use of shorter pulses to significantly increase the ablation rate in tissues low in collagen. When planning the treatment of collagenous tissues, the BHD1 metric – a product of the number of pulses per point and the pulse duration – can be used as a benchmark set of exposure parameters.

Credit authorship contribution statement

Ekaterina Ponomarchuk: Writing - Original Draft, Investigation, Formal analysis, Visualization, Software, Validation, Data Curation, Funding acquisition. **Gilles Thomas:** Investigation, Software, Data Curation, Validation, Resources, Writing - Review & Editing. **Minho Song:** Investigation, Software, Data Curation, Resources, Validation, Writing - Review & Editing. **Alisa Krokhmal:** Software, Formal analysis, Writing – review & editing, Funding acquisition. **Anastasia Kvashennikova:** Formal analysis, Writing – review & editing, Funding acquisition. **Yak-Nam Wang:** Resources, Writing – review & editing. **Vera Khokhlova:** Conceptualization, Methodology, Supervision, Funding acquisition, Writing - Review & Editing, Project administration. **Tatiana Khokhlova:** Conceptualization, Methodology, Supervision, Project administration, Funding acquisition, Investigation, Validation, Writing - Review & Editing.

Declaration of Competing Interest

The authors declare that they have no known competing financial interests or personal relationships that could have appeared to influence the work reported in this paper.

Data availability

No data was used for the research described in the article.

Acknowledgement

This work was supported by Russian Science Foundation [grant 20-12-00145] and student fellowships from Focused Ultrasound Foundation, Foundation for the Advancement of Theoretical Physics and Mathematics "BASIS" [20-2-10-10-1], and Nonprofit Foundation for the Development of Science and Education "Intellect".

References

[1] Khokhlova, V. A., Fowlkes, J. B., Roberts, W. W., Schade, G. R., Xu, Z., Khokhlova, T. D., Hall, T. L., Maxwell, A. D., Wang, Y. N., Cain, C. A. Histotripsy methods in mechanical disintegration of tissue: towards clinical applications. Int. J. Hyperthermia. 31 (2015) 145–162. https://doi.org/10.3109/02656736.2015.1007538

[2] Xu, Z., Hall, T. L., Vlaisavljevich, E., Lee, F. T. Jr. Histotripsy: the first noninvasive, non-ionizing, non-thermal ablation technique based on ultrasound. Int. J. Hyperthermia. 38 (2021) 561–575. https://doi.org/doi:10.1080/02656736.2021.1905189

[3] Simon, J. C., Sapozhnikov, O. A., Khokhlova, V. A., Wang, Y. N., Crum, L. A., Bailey, M. R. Ultrasonic atomization of tissue and its role in tissue fractionation by high intensity focused ultrasound. Phys. Med. Biol. 57 (2012) 8061–8078. https://doi.org/10.1088/0031-9155/57/23/8061

[4] Pahk, K. J., de Andrade, M. O., Gélat, P., Kim, H., Saffari, N. Mechanical damage induced by the appearance of rectified bubble growth in a viscoelastic medium during boiling histotripsy exposure. Ultrason. Sonochem. 53 (2019) 164–177. https://doi.org/10.1016/j.ultsonch.2019.01.001

[5] Pahk, K. J., Lee, S., Gélat, P., de Andrade, M. O., Saffari, N. The interaction of shockwaves with a vapour bubble in boiling histotripsy: The shock scattering effect. Ultrason. Sonochem. 70 (2021) 105312. https://doi.org/10.1016/j.ultsonch.2020.105312

[6] Matula, T. J., Wang, Y. N., Khokhlova, T., Leotta, D. F., Kucewicz, J., Brayman, A. A., Bruce, M., Maxwell, A. D., MacConaghy, B. E., Thomas, G., Chernikov, V. P., Buravkov, S. V., Khokhlova, V. A., Richmond, K., Chan, K., Monsky, W. Treating porcine abscesses with histotripsy: a pilot study. Ultrasound. Med. Biol. 47 (2021) 603–619. https://doi.org/10.1016/j.ultrasmedbio.2020.10.011

[7] Ponomarchuk, E. M., Rosnitskiy, P. B., Khokhlova, T. D., Buravkov, S. V., Tsysar, S. A., Karzova, M. M., Tumanova, K. D., Kunturova, A. V., Wang, Y. N., Sapozhnikov, O. A., Trakhtman, P. E., Starostin, N. N., Khokhlova, V. A. Ultrastructural analysis of volumetric histotripsy bio-effects in large human hematomas. Ultrasound. Med. Biol. 47 (2021) 2608–2621. https://doi.org/10.1016/j.ultrasmedbio.2021.05.002

[8] Chevillet, J. R., Khokhlova, T. D., Giraldez, M. D., Schade, G. R., Starr, F., Wang, Y. N., Gallichotte, E. N., Wang, K., Hwang, J. H., Tewari, M. Release of cell-free microrna tumor biomarkers into the blood circulation with pulsed focused ultrasound: a noninvasive, anatomically localized, molecular liquid biopsy. Radiology. 283 (2017) 158–167. https://doi.org/10.1148/radiol.2016160024

[9] Van den Bijgaart, R. J. E., Mekers, V. E., Schuurmans, F., Raaijmakers, T. K., Wassink, M., Veltien, A., Dumont, E., Heerschap, A., Fütterer, J. J., Adema, G. J. Mechanical high-intensity focused ultrasound creates unique tumor debris enhancing dendritic cell-induced T cell activation. Front. Immunol. 13 (2022) 1038347. https://doi.org/10.3389/fimmu.2022.1038347

[10] Rosnitskiy, P. B., Tsysar, S. A., Karzova, M. M., Buravkov, S. V., Malkov, P. G., Danilova, N. V., Ponomarchuk, E. M., Sapozhnikov, O. A., Khokhlova, T. D., Schade, G. R., Maxwell, A. D., Wang, Y. N., Kadrev, A. V., Chernyaev, A. L., Okhobotov, D. A., Kamalov, A. A., Khokhlova, V. A. Pilot ex vivo study on non-thermal ablation of human prostate adenocarcinoma tissue using boiling histotripsy. Ultrasonics. 133 (2023) 107029. https://doi.org/10.1016/j.ultras.2023.107029

[11] Ponomarchuk, E. M., Hunter, C., Song, M., Khokhlova, V. A., Sapozhnikov, O. A., Yuldashev, P. V., Khokhlova, T. D. Mechanical damage thresholds for hematomas near gas-containing bodies in pulsed HIFU fields. Phys. Med. Biol. 67 (2022) 215007. https://doi.org/10.1088/1361-6560/ac96c7

[12] Khokhlova, T. D., Haider, Y. A., Maxwell, A. D., Kreider, W., Bailey, M. R., Khokhlova, V. A. Dependence of boiling histotripsy treatment efficiency on hifu frequency and focal pressure levels. Ultrasound. Med. Biol. 43 (2017) 1975–1985. https://doi.org/10.1016/j.ultrasmedbio.2017.04.030

[13] Khokhlova, T. D., Canney, M. S., Khokhlova, V. A., Sapozhnikov, O. A., Crum, L. A., Bailey, M. R. Controlled tissue emulsification produced by high intensity focused ultrasound shock waves and millisecond boiling. J. Acoust. Soc. Am. 130 (2011) 3498–3510. https://doi.org/10.1121/1.3626152

[14] Khokhlova, T. D., Kucewicz, J. C., Ponomarchuk, E. M., Hunter, C., Bruce, M., Khokhlova, V. A., Matula, T. J., Monsky, W. Effect of stiffness of large extravascular hematomas on their susceptibility to boiling histotripsy liquefaction in vitro. Ultrasound. Med. Biol. 46 (2020) 2007–2016. https://doi.org/10.1016/j.ultrasmedbio.2020.04.023

[15] Khokhlova, T. D., Schade, G. R., Wang, Y. N., Buravkov, S. V., Chernikov, V. P., Simon, J. C., Starr, F., Maxwell, A. D., Bailey, M. R., Kreider, W., Khokhlova, V. A. Pilot in vivo studies on transcutaneous boiling histotripsy in porcine liver and kidney. Sci. Rep. 9 (2019) 20176. https://doi.org/10.1038/s41598-019-56658-7

[16] Zhou, Y., Wang, X. Effect of pulse duration and pulse repetition frequency of cavitation histotripsy on erosion at the surface of soft material. Ultrasonics. 84 (2018) 296–309. https://doi.org/10.1016/j.ultras.2017.11.012

[17] Xu, J., Bigelow, T. A., Lee, H. Effect of pulse repetition frequency and scan step size on the dimensions of the lesions formed in agar by HIFU histotripsy. Ultrasonics. 53 (2013) 889–896. https://doi.org/10.1016/j.ultras.2012.12.011

[18] Wang, Y. N., Khokhlova, T. D., Buravkov, S., Chernikov, V., Kreider, W., Partanen, A., Farr, N., Maxwell, A., Schade, G. R., Khokhlova, V. A. Mechanical decellularization of tissue volumes using boiling histotripsy. Phys. Med. Biol. 63 (2018) 235023. https://doi.org/10.1088/1361-6560/aaef16

[19] Vlaisavljevich, E., Kim, Y., Owens, G., Roberts, W., Cain, C., Xu, Z. Effects of tissue mechanical properties on susceptibility to histotripsy-induced tissue damage. Phys. Med. Biol. 59 (2014) 253–270. https://doi.org/10.1088/0031-9155/59/2/253

[20] Khokhlova, V. A., Rosnitskiy, P. B., Tsysar, S. A., Buravkov, S. V., Ponomarchuk, E. M., Sapozhnikov, O. A., Karzova, M. M., Khokhlova, T. D., Maxwell, A. D., Wang, Y. N., Kadrev, A. V., Chernyaev, A. L., Chernikov, V. P., Okhobotov, D. A., Kamalov, A. A., Schade, G. R. Initial assessment of boiling histotripsy for mechanical ablation of ex vivo human prostate tissue. Ultrasound. Med. Biol. 49 (2023) 62–71. https://doi.org/10.1016/j.ultrasmedbio.2022.07.014

[21] Pahk, K. J., Mohammad, G. H., Malago, M., Saffari, N., Dhar, D. K. A novel approach to ultrasound-mediated tissue decellularization and intra-hepatic cell delivery in rats. Ultrasound. Med. Biol. 42 (2016) 1958–1967. https://doi.org/10.1016/j.ultrasmedbio.2016.03.020

[22] Smallcomb, M., Simon, J. C. High intensity focused ultrasound atomization and erosion in healthy and tendinopathic tendons. Phys. Med. Biol. 68 (2023) 025005. https://doi.org/10.1088/1361-6560/aca9b7

[23] Bawiec, C. R., Khokhlova, T. D., Sapozhnikov, O. A., Rosnitskiy, P. B., Cunitz, B. W., Ghanem, M. A., Hunter, C., Kreider, W., Schade, G. R., Yuldashev, P. V., Khokhlova, V. A. A prototype therapy system for boiling histotripsy in abdominal targets based on a 256-element spiral array. IEEE Trans. Ultrason. Ferroelectr. Freq. Control. 68 (2021) 1496–1510. https://doi.org/10.1109/TUFFC.2020.3036580

[24] Sapareto, S. A., Dewey, W. C. Thermal dose determination in cancer therapy. Int. J. Radiat. Oncol. Biol. Phys. 10 (1984) 787–800. https://doi.org/10.1016/0360-3016(84)90379-1

[25] Brady, L., Wang, Y. N., Rombokas, E., Ledoux, W. R. Comparison of texture-based classification and deep learning for plantar soft tissue histology segmentation. Comput. Biol. Med. 134 (2021) 104491. https://doi.org/10.1016/j.compbiomed.2021.104491

[26] Homeyer, A., Schenk, A., Arlt, J., Dahmen, U., Dirsch, O., Hahn, H. K. Practical quantification of necrosis in histological whole-slide images Comput. Med. Imaging. Graph. 37 (2013) 313–322. https://doi.org/10.1016/j.compmedimag.2013.05.002

[27] Rangraz, P., Behnam, H., Shakhssalim, N., Tavakkoli, J. A feed-forward neural network algorithm to detect thermal lesions induced by high intensity focused ultrasound in tissue. J. Med. Signals Sens. 2 (2012) 192–202. PMCID: PMC3662102

[28] Li, J., Sarma, K. V., Chung Ho, K., Gertych, A., Knudsen, B. S., Arnold, C. W. A multi-scale u-net for semantic segmentation of histological images from radical prostatectomies. AMIA Annu. Symp. Proc. (2018) 1140–1148. PMCID: PMC5977596

[29] Kalapahar, A., Silva-Rodríguez, J., Colomer, A., López-Mir, F., Naranjo, V. Gleason grading of histology prostate images through semantic segmentation via residual u-net. ICIP. (2020) 2501–2505. https://doi.org/10.1109/ICIP40778.2020.9191250

[30] Fu X, Liu T, Xiong Z, Smaill BH, Stiles MK, Zhao J. Segmentation of histological images and fibrosis identification with a convolutional neural network. Comput. Biol Med. 98 2018 147–158. https://doi.org/10.1016/j.compbiomed.2018.05.015

[31] Bessonova, O. V., Khokhlova, V. A., Canney, M. S., Bailey, M. R., Crum, L. A. A derating method for therapeutic applications of high intensity focused ultrasound. Acoust. Phys. 56 (2010) 354–363. https://doi.org/10.1134/s1063771010030140

[32] Canney, M. S., Khokhlova, V. A., Bessonova, O. V., Bailey, M. R., Crum, L. A. Shock-induced heating and millisecond boiling in gels and tissue due to high intensity focused ultrasound. Ultrasound. Med. Biol. 36 (2010) 250–267. https://doi.org/10.1016/j.ultrasmedbio.2009.09.010

[33] Duck, F. Physical properties of tissue: A comprehensive reference book. London: Academic Press, 1990.

[34] Mohammadi, A., Bianchi, L., Asadi, S., Saccomandi, P. Measurement of ex vivo liver, brain and pancreas thermal properties as function of temperature. Sensors. 21 (2021) 4236. https://doi.org/10.3390/s21124236

[35] Niehues, S. M., Unger, J. K., Malinowski, M., Neymeyer, J., Hamm, B., Stockmann, M. Liver volume measurement: reason of the difference between in vivo CT-volumetry and intraoperative ex vivo determination and how to cope it. Eur. J. Med. Res. 15 (2010) 345–350. https://doi.org/10.1186/2047-783x-15-8-345

[36] He K., Zhang X., Ren S., Sun J. Deep residual learning for image recognition. 2016 IEEE CVPR, (2016) 770–778. https://doi.org/10.1109/CVPR.2016.90

[37] Xu W., Fu Y.L., Zhu D. ResNet and its application to medical image processing: Research progress and challenges. Comput Methods Programs Biomed. 240 (2023) 107660. https://doi.org/10.1016/j.cmpb.2023.107660

[38] Singh, J., Sharma, A., Sarma, K., Suri, S. Malik, M. R. A quantitative histological study of the liver of pig (Sus scrofa). Indian Vet. J. 94 (2017) 14–16.

[39] Larson, A., Chin, M. T. A method for cryopreservation and single nucleus RNA-sequencing of normal adult human interventricular septum myocardium tissue reveals cellular diversity and function. BMC Med. Genom. 14 (2021) 161. https://doi.org/10.1186/s12920-021-01011-z

[40] Tran, T., Sundaram, C. P., Bahler, C. D., Eble, J. N., Grignon, D. J., Monn, M. F., Simper, N. B., Cheng, L. Correcting the shrinkage effects of formalin fixation and tissue processing for renal tumors: toward standardization of pathological reporting of tumor size. J. Cancer. 6 (2015) 759–766. https://doi.org/10.7150/jca.12094

[41] Williams, R. P., Simon, J. C., Khokhlova, V. A., Sapozhnikov, O. A., Khokhlova, T. D. The histotripsy spectrum: differences and similarities in techniques and instrumentation. Int. J. Hyperthermia. 40 (2023) 2233720. https://doi.org/10.1080/02656736.2023.2233720

[42] Song, M., Thomas, G. P. L., Khokhlova, V. A., Sapozhnikov, O. A., Bailey, M. R., Maxwell, A. D., Yuldashev, P. V., Khokhlova, T. D. Quantitative assessment of boiling histotripsy progression based on color doppler measurements. IEEE Trans. Ultrason. Ferroelectr. Freq. Control. 69 (2022) 3255–3269. https://doi.org/10.1109/TUFFC.2022.3212266